AIAA JOURNAL
Vol. 36, No. 1, January 1998

Evaluation of Explicit Algebraic Reynolds-Stress Models for Separated Supersonic Flows

Donald P. Rizzetta*
U.S. Air Force Research Laboratory, Wright–Patterson Air Force Base, Ohio 45433-7913

High-Reynolds-number supersonic flowfields were generated numerically to assess the performance of three explicit algebraic Reynolds-stress turbulence models. The configurations consist of a shock/boundary-layer interaction and a 24-deg compression ramp, both of which exhibit an appreciable region of separated flow. Solutions were also obtained using standard zero-equation and k–ϵ models. Details of the computations are summarized, and the accuracy of numerical results is established via grid resolution studies. Comparisons are made with experimental data in terms of surface pressure and skin friction, as well as off-surface profiles of mean velocity and components of the Reynolds-stress tensor. For the flows considered here, it is found that the algebraic-stress models offer little improvement over existing closures.

Nomenclature

C_f	= skin-friction coefficient
k	= turbulence kinetic energy
l	= reference length, 1.0 m
M	= Mach number
p	= static pressure
Re	= reference Reynolds number
u	= Cartesian velocity component in x direction
$\overline{u'u'}$, $\overline{v'v'}$, $\overline{u'v'}$	= components of the Reynolds-stress tensor
x, y	= nondimensional Cartesian coordinates in streamwise and vertical directions
y^+	= law-of-the-wall coordinate
Δx, Δy	= mesh spacing in streamwise and vertical directions
δ_0	= undisturbed boundary-layer thickness
δ^*	= displacement thickness
ϵ	= turbulence energy dissipation
θ	= momentum thickness

Subscripts

w	= wall value
0	= upstream undisturbed value
∞	= freestream value

Introduction

ADVANCES in numerical algorithms and increases in the speed and storage capacity of computing machines have made it possible to simulate intricate high-Reynolds-number flowfields about large-scale configurations. Because it is still not feasible to resolve the finest scales inherent in such flows, effects of turbulence must be accounted for through modeling. The utility of these computations is, therefore, limited by the ability of turbulence models to accurately reproduce dominant features of the flow physics.

Most common models employ the Boussinesq hypothesis, whereby turbulent stresses in the averaged momentum and energy equations are assumed to equal the product of an effective isotropic viscosity coefficient and the strain rate of the mean flow. The eddy-viscosity concept has gained popularity, particularly for engineering use, because of its ease of implementation and its favorable performance over a wide range of applications. Eddy-viscosity coefficients may be obtained by a direct dependence on mean flow quantities (algebraic), or by solving auxiliary field equations for combinations of the turbulent velocity and time scales, which account for history effects of the flow.

Models that prescribe transport equations for each component of the turbulent stress tensor offer the highest level of generality that is available for the solution of mean flow equations. These models eliminate the assumption of a direct proportion between turbulent stresses and the mean strain rate and account for anisotropy. Many unknown turbulent quantities, however, are required for a complete description of the transport equations, and these are generally obtained by assuming that the turbulence is locally homogeneous and in equilibrium. Moreover, computing cost and numerical stability problems associated with solving these equations[1] makes their application in complicated situations impractical.

Although eddy-viscosity models perform well for many types of flows, they fail to adequately describe a number of physical phenomena including streamline curvature, rotational strains, buoyancy, strong adverse pressure gradients, and turbulent anisotropy. An approach that attempts to alleviate these shortcomings adopts an explicit nonlinear connection between the turbulent stresses and the rate-of-strain and vorticity tensors of the mean flow. Based on the analysis of Pope,[2] who employed the Reynolds-stress equation of Launder et al.[3] along with the algebraic form of Rodi,[4] these models are commonly used in conjunction with two subsidiary transport equations and have the potential for improved performance without the complexity or computational overhead associated with complete Reynolds-stress equations.

Several nonlinear eddy-viscosity models have been proposed,[5–8] but currently there are three popular variants of the explicit algebraic Reynolds-stress description.[9] These consist of the models due to Gatski and Speziale,[1,10–13] to Shih et al.,[14] and to Craft et al.[15,16] Whereas some transonic solutions have been reported for the Gatski–Speziale[1,12,13] representation, most applications of these models have been for subsonic flows. And although closure of the models is highly predicated on incompressible results, the basic formulation, particularly that of the auxiliary equations, should remain valid for external Mach numbers less than five.[13]

The purpose of the present work is to provide a critical evaluation of explicit algebraic Reynolds-stress turbulence models for separated supersonic flows. This is done by performing computations to simulate two fundamental configurations consisting of the impingement of an oblique shock wave with the boundary layer over a flat surface and of the flow past a 24-deg, two-dimensional compression ramp. The flowfields, shown schematically in Fig. 1, are characterized by inviscid/viscous interactions producing strong adverse pressure gradients and substantial regions of reverse streamwise velocity and represent situations where isotropic eddy-viscosity models typically fail to adequately reproduce many physical details of the flow.

Received March 28, 1997; presented as Paper 97-2125 at the AIAA 28th Fluid Dynamics Conference, Snowmass Village, CO, June 29–July 2, 1997; revision received Sept. 17, 1997; accepted for publication Sept. 17, 1997.

*Research Aerospace Engineer, Computational Fluid Dynamics Research Branch, Aeromechanics Division. Associate Fellow AIAA.

Table 1 Designation of turbulence models

Model	Closure	Designation
Baldwin–Lomax [17]	Algebraic (zero-equation)	BL
Jones–Launder [18,19]	Two-equation (k–ϵ)	JL
Speziale–Abid [11]	Two-equation (k–ϵ)	SA
Gatski–Speziale [1,10–13]	Algebraic Reynolds stress	GS-ARS
Shih–Zhu–Lumley [14]	Algebraic Reynolds stress	SZL-ARS
Craft–Launder–Suga [15,16]	Algebraic Reynolds stress	CLS-ARS

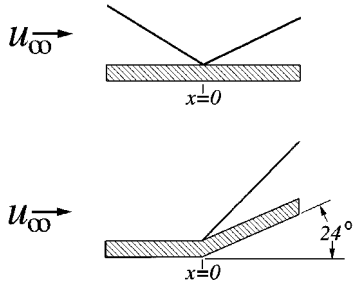

Fig. 1 Configuration for the shock/boundary-layer interaction and compression ramp flows.

In addition to the aforementioned turbulent stress models, the widely used Baldwin–Lomax [17] algebraic eddy viscosity and the k–ϵ formulations of Jones and Launder[18,19] and Speziale and Abid[11] are also considered for comparison. It is convenient to devise a notational designation for each model, which may be found in Table 1. The governing equations and numerical procedure are summarized, and details of the computations are presented. Grid resolution studies are provided in each case to ensure numerical accuracy. Solutions from all models are compared to each other and with existing experimental data for surface pressure and-skin friction distributions and off-surface profiles of mean velocity and components of the Reynolds-stress tensor.

Governing Equations

The governing equations were taken to be the unsteady two-dimensional compressible mass-averaged turbulent Navier–Stokes equations, written in nondimensional variables and expressed in strong-conservation form. Effects of turbulence were accounted for by specifying a turbulent Prandtl number of 0.90 and by use of an effective viscosity coefficient for the algebraic and two-equation closures, or by contributions to the Reynolds-stress tensor. The Sutherland law for the molecular viscosity coefficient and the perfect gas relationship were also utilized, and Stokes' hypothesis for the bulk viscosity coefficient was invoked. Complete details of the governing equations and associated boundary conditions, including those for k–ϵ forms and Reynolds-stress models, are documented in Ref. 20 but have been omitted here for brevity.

The Jones–Launder (JL) k–ϵ model, which has been applied to a number of supersonic flow problems,[21–25] includes low-Reynolds-number terms to improve near-wall modeling and does not require the use of any predefined length scales. In addition, because the equation for ϵ is formulated in terms of the difference between the dissipation rate of the turbulent kinetic energy and that of homogeneous turbulence, both k and ϵ vanish at solid surfaces, thereby facilitating application of boundary conditions for flows about geometrically complex configurations. Although the Speziale–Abid (SA) model contains no low-Reynolds-number terms, it is designed to remove the singularity in the dissipation rate equation at solid surfaces, so that the k–ϵ equations may be integrated directly to wall boundaries.[1,11–13]

For certain supersonic applications, it has been useful to include corrections to the k–ϵ equations that account for dilatation–dissipation and/or pressure-dilatation fluctuation. Often, such corrections can degrade performance in near-wall regions of attached flows[9] and, thus, were not incorporated in the present computations.

In principle, each algebraic stress model can be used in conjunction with any suitable two-equation representation. However, model originators have assigned specific k–ϵ forms that then determine the choice of constants, parameters, and functions for their use. The SA k–ϵ equations are associated with the Gatski–Speziale algebraic Reynolds-stress (GS-ARS) model. It is recommended that the Shih–Zhu–Lumley algebraic Reynolds-stress (SZL-ARS) model be used together with a standard high-Reynolds-number form of the k–ϵ equations.[14] This implementation precludes integration of the equations directly to solid boundaries and necessitates the use of wall functions. As an alternative, the SA k–ϵ equations were combined with the SZL-ARS model to provide a consistent treatment of the wall-bounded flows considered here. Apart from the mentioned removal of the singularity in the ϵ equation at solid surfaces and a slight variation in one constant, the SA model is identical to the standard high-Reynolds-number k–ϵ form. The suitability of this approach was validated by computation of several flat-plate flows.

The Craft–Launder–Suga algebraic Reynolds-stress (CLS-ARS) model employs the JL k–ϵ set with a modified low-Reynolds-number term. A length-scale correction is also utilized to enhance near-wall performance in separation and stagnation regions.[16] Note that the GS-ARS and SZL-ARS models are second-order closures containing Reynolds stresses, which are quadratic in the strain rate and vorticity, whereas the CLS-ARS model includes third-order cubic terms.

Numerical Procedure

Steady-state solutions to the governing equations were obtained numerically by the implicit approximately factored finite difference algorithm of Beam and Warming,[26] which has evolved as an efficient tool for generating solutions to a wide variety of complex fluid flow problems. First-order accurate Euler-implicit time differencing was used to represent temporal derivatives. Inviscid fluxes considered in the explicit portion of the algorithm were evaluated by Roe's upwind-biased scheme[27] using the MUSCL approach[28] with van Leer's harmonic limiter[29] to achieve third-order spatial accuracy. Second-order accurate central differences were used to approximate viscous terms.

The implicit segment of the algorithm employed second-order accurate centered differencing for all spatial derivatives and incorporated nonlinear artificial dissipation[30] to augment stability. As the steady state is approached, degradation in the solution due to artificial dissipation becomes negligible. Only the contributions of the Reynolds stresses to the mean flow equations that are linear in the strain rate were treated implicitly.

Solutions to the k–ϵ equations were decoupled from the Navier–Stokes equations by lagging their values from the mean flow variables. In addition, k and ϵ were uncoupled from each other by also evaluating source terms explicitly. It has been shown that this technique is effective for a number of practical flow applications.[22–25] For some computations, Newton-like subiterations[31] were used to augment stability and relieve stiffness associated with solution of the k–ϵ equations.

Stated features of the numerical algorithm are embodied in an existing fully vectorized computer code FDL2DI, which has proven to be reliable for both steady and unsteady Navier–Stokes calculations. After installation of each stress model in the code, validation was performed by comparing skin-friction and velocity profiles in the logarithmic region with theoretical values for both subsonic and supersonic flat-plate flows.

Results

Experimental conditions for the shock/boundary-layer interaction and compression ramp flows are provided in Table 2. These configurations were selected as representative examples of basic supersonic situations in which streamwise separation is present. Because less turning of the flow occurs for the shock/boundary-layer interaction, consideration of both flows may be useful in assessing the ability of the turbulence models to correctly account for streamline curvature.

Shock/Boundary-Layer Interaction

Measurements of the shock/boundary-layer interaction experiment are detailed in a series of investigations that are reported in Refs. 32–35. These data have previously been used for performance assessment of zero-, one-, and two-equation models of turbulence.[36]

Table 2 Flow conditions

Case	M_∞	Re	T_w
Shock/boundary layer	2.90	5.73×10^7/m	2.682
Compression ramp	2.94	3.75×10^7/m	Adiabatic

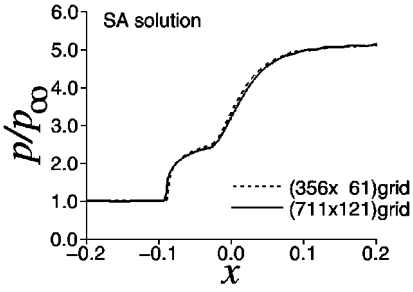

Fig. 2 Effect of grid resolution on the surface static pressure distribution of the SA solution for the shock/boundary-layer interaction.

To establish profiles of dependent variables at the upstream inflow boundary of the computational domain, flat-plate solutions were obtained for all turbulence models. From the plate leading edge, the streamwise extent of these calculations was taken to be sufficiently long so that boundary-layer profiles corresponding approximately to those of the experiment could be obtained. The displacement thickness δ^* and momentum thickness θ were used as criteria to evaluate the profiles. For any specific turbulence model, it was not possible to simultaneously obtain values of δ^* and θ that coincided with those of the experiment. Profiles were selected at streamwise locations on the plate at the midpoint between those stations where numerical values of δ^* matched the experiment and those where θ was matched. Computed values of δ^* and θ deviate from the experiment by less than 3.5% for each model. Mach number profiles from the flat-plate solutions are compared to experimental measurements[32] for the undisturbed flow upstream of the interaction region in Ref. 20.

Because of the simplicity of the configuration, a Cartesian mesh consisting of (711×121) points in the streamwise and vertical directions, respectively, was constructed about the interaction region. The grid spacing was uniform in the streamwise direction with $\Delta x \approx 7.61 \times 10^{-4}$ and at the wall $\Delta y = 10^{-6}$. This resolution resulted in a value of $y^+ < 0.4$ at the first mesh point above the solid surface in the upstream profiles for all turbulence models. Geometric stretching was employed away from the wall to a distance of $y = 0.16$. An oblique shock wave was initiated at a distance of 10 x-grid lines downstream from the forward boundary at the top of the computational domain, by specifying oblique-shock turning conditions for the dependent variables corresponding to a wedge angle of 13 deg. This duplicated the experimental configuration, which employed a shock generator with the same angle. The origin of the coordinate system was selected as the point where the incident oblique shock wave intersects the wall (see Fig. 1), based on inviscid theory, consistent with the experimental description.

Flowfields were initialized using the upstream profiles for each turbulence model and integrated in time until the steady state was attained. It was established that this condition had been achieved by monitoring the total variation in all variables over the entire computational domain, as well as surface pressure and skin friction. To study the adequacy of spatial resolution, solutions for all models were also computed on a (356×61) grid, which was formed by removing every other point in each coordinate direction from the (711×121) mesh. Surface pressure distributions on both grids for the SA model are presented in Fig. 2. These results were displayed because they exhibited the largest variation between solutions on the two meshes for any of the models considered. In particular, on the scale of Fig. 2 no difference between results on these grids could be discerned for any of the algebraic-stress models. Other quantities, such as skin friction and mean velocity, showed grid sensitivity that was similar to that of the pressure. The results to follow are from fine-grid computations.

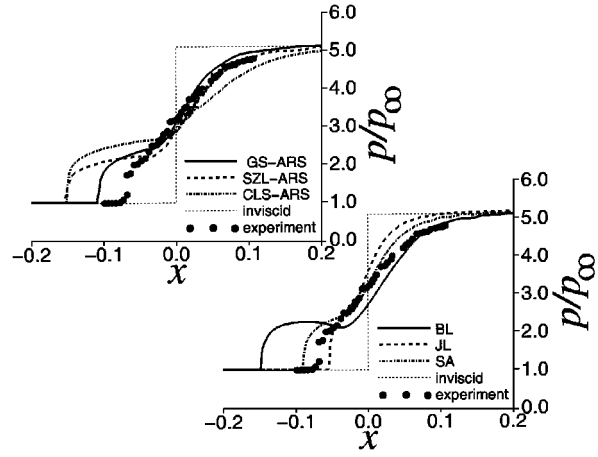

Fig. 3 Surface static pressure distributions for the shock/boundary-layer interaction.

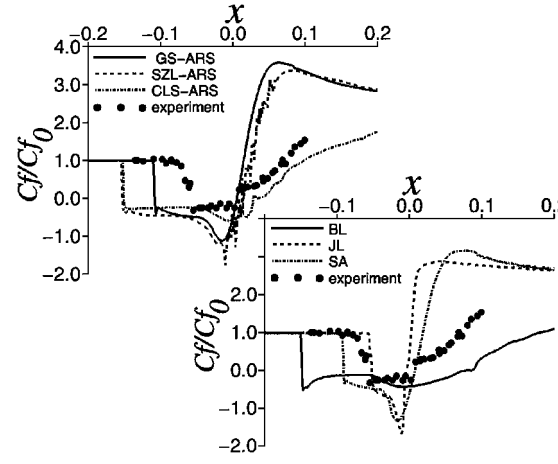

Fig. 4 Skin-friction coefficient distributions for the shock/boundary-layer interaction.

Surface pressure distributions are compared to experimental data[32] in Fig. 3. The Baldwin–Lomax (BL) model is seen to perform poorly, which is typical for such flows. Both the JL and SA models provide better results than the BL model, though neither is outstanding. Of the stress models, the GS-ARS has the best performance. All of the stress models generate a larger upstream interaction than indicated in the experiment. Note that the GS-ARS solution, used in conjunction with the SA k–ϵ equations, compares slightly less favorably with the data than does the SA result alone.

Corresponding skin-friction distributions,[32] where C_f has been normalized by its upstream undisturbed value, are shown in Fig. 4. Here it is seen that the JL model closely duplicates the length of the separation region, but poorly predicts the downstream recovery. All other models generate regions of reversed flow that are larger than those of the experiment, especially upstream of $x = 0$. The CLS-ARS model appears to best simulate the behavior downstream.

Because the streamwise extent of flow separation was not well represented by the majority of the models, detailed profile measurements at fixed x locations cannot be expected to compare favorably with the computations. Mean streamwise velocity profiles[34] are displayed in Figs. 5 and 6. As anticipated, only the JL model provides satisfactory agreement with the data over the entire range of the comparison. The large vertical extent of the boundary layers generated by other models is apparent. Of the Reynolds-stress formulations, the GS-ARS model produced the best results, particularly for $x > 0$.

Profiles of the Reynolds-stress component $\overline{u'u'}$ (Ref. 34) are given in Fig. 7. It is evident that the near-wall behavior at upstream stations is not well simulated by any of the models. Downstream, the GS-ARS model performs better than the others. At $x = 0.043$, all models agree with the data as equilibrium conditions are approached. Corresponding profiles of $\overline{v'v'}$ (Ref. 33) were only measured at the five stations indicated in Fig. 8. Once again, the GS-ARS model compares

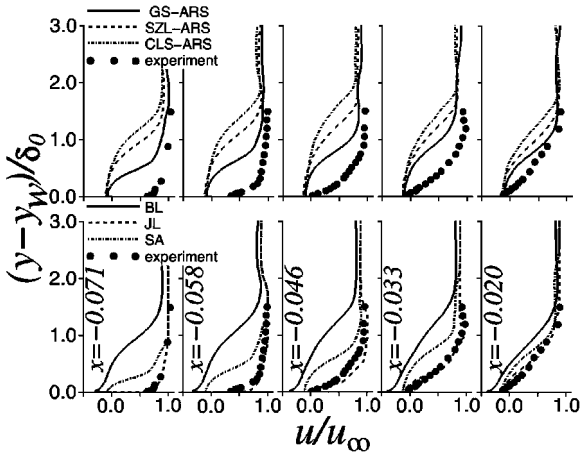

Fig. 5 Mean velocity profiles at upstream stations for the shock/boundary-layer interaction.

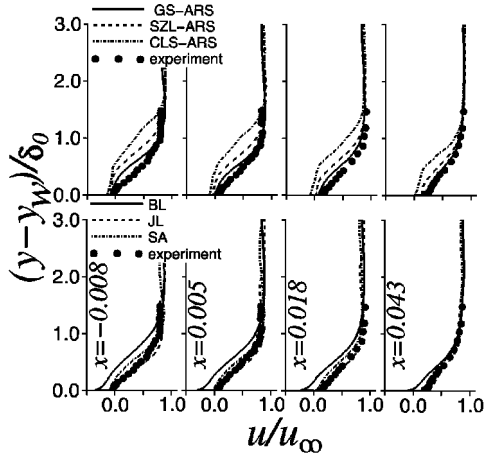

Fig. 6 Mean velocity profiles at downstream stations for the shock/boundary-layer interaction.

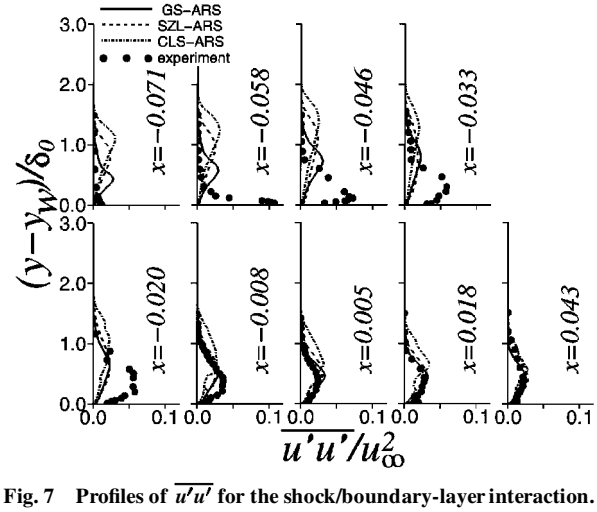

Fig. 7 Profiles of $\overline{u'u'}$ for the shock/boundary-layer interaction.

reasonably well with the data. Solutions from the isotropic eddy-viscosity models (BL, JL, SA) produced values of $\overline{u'u'}$ and $\overline{v'v'}$ that were considerably smaller than those in Figs. 7 and 8. Consequently, these profiles could not be observed in the figures and, therefore, are not presented.

Compression Ramp

Flow conditions for the 24-deg compression ramp experiment of Kuntz et al.[37] are given in Table 2. Complete results of the laser Doppler velocimetry measurements are available in the database of Ref. 38. Similar to the shock/boundary-layer interaction, flat-

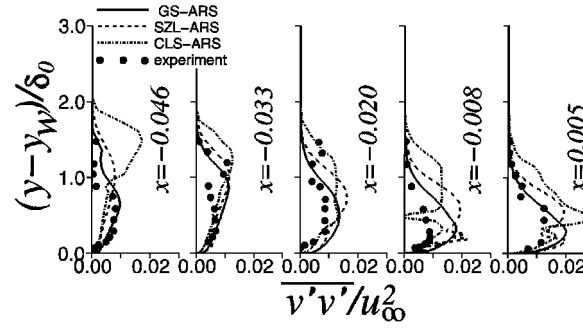

Fig. 8 Profiles of $\overline{v'v'}$ for the shock/boundary-layer interaction.

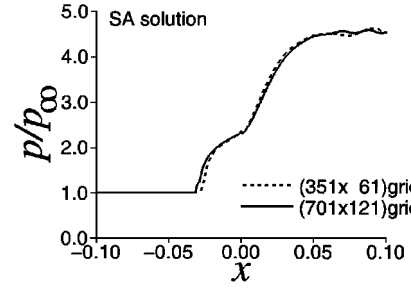

Fig. 9 Effect of grid resolution on the surface static pressure distribution of the SA solution for the compression ramp.

plate computations were performed to obtain profiles of dependent variables at the upstream inflow boundary. Experimental values of δ^* and θ were again used to establish acceptable numerical profiles. In this instance, the undisturbed flow experimental data were collected at the corner streamwise location, but with the ramp angle set to 0 deg. As noted earlier, experimental values of both δ^* and θ could not be duplicated simultaneously, but the computed values were within 6.8% of the data for all models. Velocity profiles and Reynolds-stress components from the flat-plate calculations are compared to experimental surveys in Ref. 20.

For the compression ramp computations, a simple sheared Cartesian (701 × 121) grid was used to represent the interaction flowfield. The origin coincided with the ramp corner location, and the domain was defined by $-0.1 \le x \le 0.1$. At the wall surface, $\Delta y = 10^{-6}$, and stretching established the upper boundary at a distance $y - y_w = 0.5$. Uniform streamwise spacing with $\Delta x = 2.5 \times 10^{-4}$ was employed for the upstream 75% extent of the domain. Downstream, a slight stretching to the outflow boundary was utilized. The undisturbed profiles for all turbulence models had a value of $y^+ < 0.3$ at the first mesh point above the wall.

Inflow profiles of dependent variables were extracted from the flat-plate solutions at the distance ahead of the selected undisturbed flow locations that corresponded to the relative position of the upstream boundary. Solutions for all turbulence models were obtained on both the (710 × 121) and a (351 × 61) grid system. Surface pressure distributions computed on both meshes for the SA model are presented in Fig. 9. This model was again used to indicate grid sensitivity because it resulted in the most variation between solutions on the two meshes. As in the shock/boundary-layer interaction, no differences in solutions on the two grids was observed for any of the algebraic-stress models.

Surface pressure distributions for all turbulence closures are seen in Fig. 10. Here, the SA model compares quite well with the experimental data. The comparison is less favorable for the GS-ARS result, which performs similar to the BL model. Both the SZL-ARS and CLS-ARS solutions compare poorly with the measurements. Figure 11 presents corresponding distributions of the skin friction. Only surface streak patterns, indicating the points of separation and attachment, were obtained experimentally for this configuration. It is noted in Fig. 11 that the JL solution underpredicts the length of the reversed flow region and that the SA result only slightly overpredicts this distance. All other solutions have a greater streamwise extent of separation.

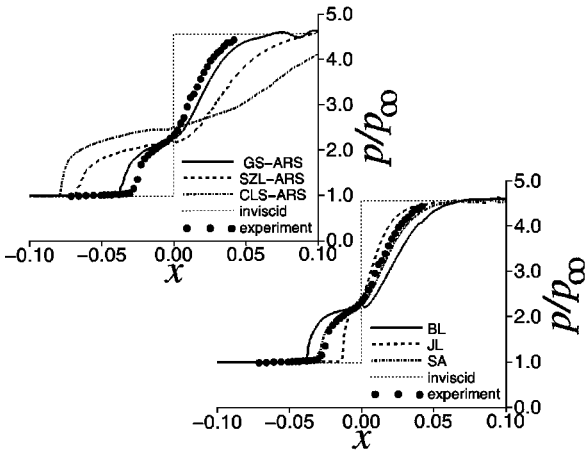

Fig. 10 Surface static pressure distributions for the compression ramp.

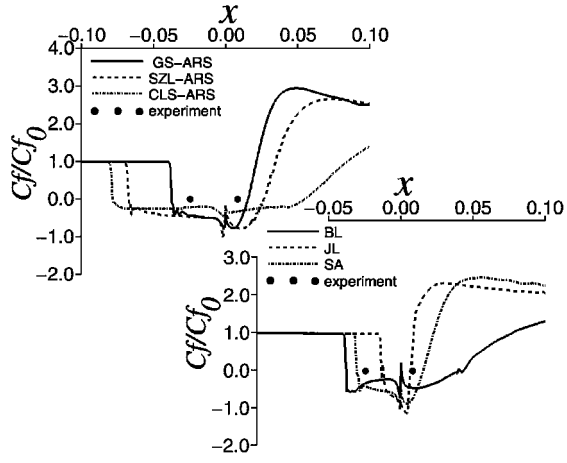

Fig. 11 Skin-friction coefficient distributions for the compression ramp.

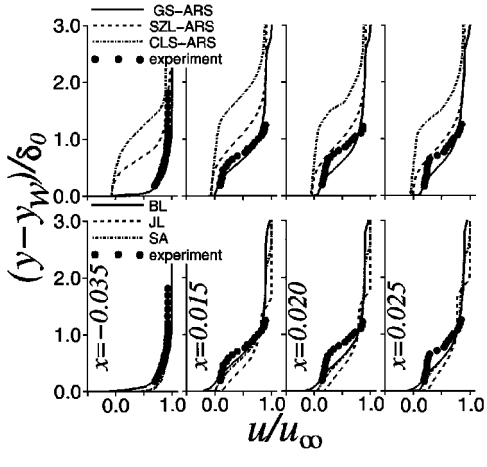

Fig. 12 Mean velocity profiles at upstream stations for the compression ramp.

Mean velocity profiles at several locations are shown in Figs. 12 and 13. At the two most upstream stations, $x = -0.035$ and 0.015, both the SA and GS-ARS solutions compare favorably with the data. The comparison for these models is also favorable at the last two downstream stations, $x = 0.035$ and 0.040. This can be attributed to the fact that these solutions most nearly reproduced the length of the separated flow region. For $x > 0.025$, the SZL-ARS result in the outer portion of the boundary layer resembles the data, but does not agree with it very well near the wall. When $x > 0.015$, the CLS-ARS profiles are much like those of the experiment, but with a different vertical displacement. Performance of the BL model is comparable to that of the SA and GS-ARS formulations.

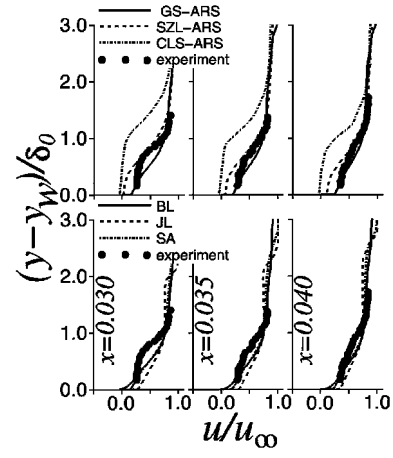

Fig. 13 Mean velocity profiles at downstream stations for the compression ramp.

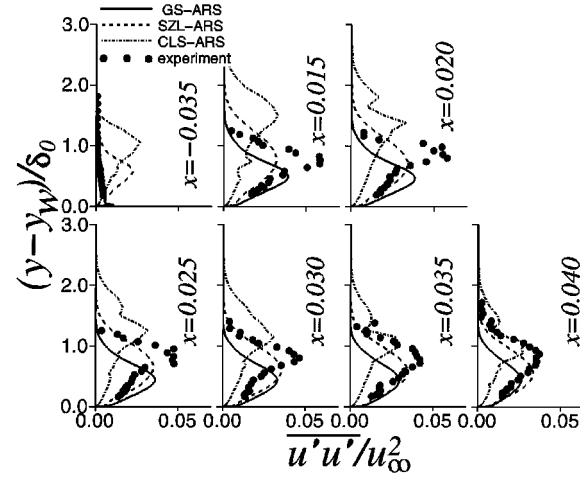

Fig. 14 Profiles of $\overline{u'u'}$ for the compression ramp.

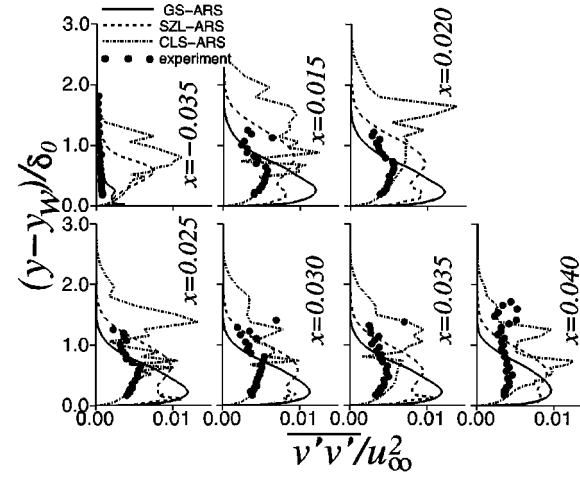

Fig. 15 Profiles of $\overline{v'v'}$ for the compression ramp.

Shown in Fig. 14 are profiles of the $\overline{u'u'}$ Reynolds-stress component. At the $x = -0.035$ station, the GS-ARS solution agrees well with the data, and it also has comparable qualitative behavior for $x = 0.015$. The CLS-ARS result appears similar in shape to the experiment at the last three downstream stations, but does not agree with it quantitatively. Corresponding profiles of the $\overline{v'v'}$ component may be found in Fig. 15. As was also the case for the shock/boundary-layer interaction, profiles of $\overline{u'u'}$ and $\overline{v'v'}$ from the isotropic eddy-viscosity models have been omitted from Figs. 14 and 15 because of the small magnitude of their values.

The final Reynolds-stress component $-\overline{u'v'}$ is given in Figs. 16 and 17. Once more, the comparison of all models with the measured

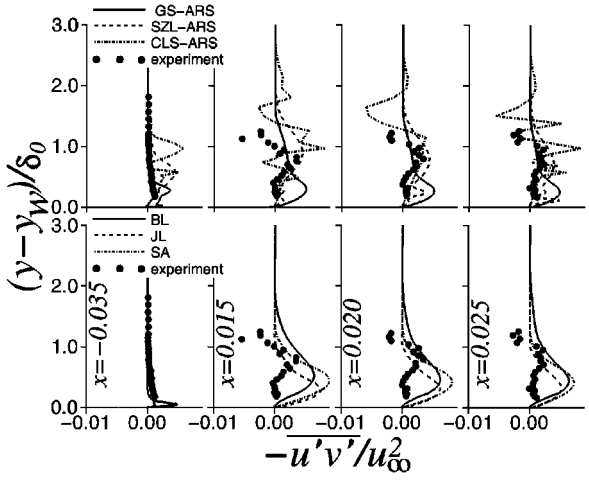

Fig. 16 Profiles of $-\overline{u'v'}$ at upstream stations for the compression ramp.

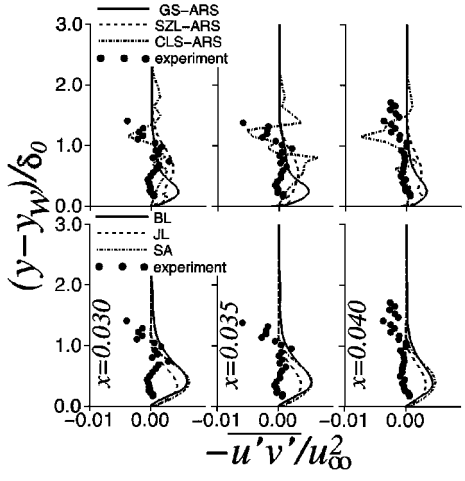

Fig. 17 Profiles of $-\overline{u'v'}$ at downstream stations for the compression ramp.

data is poor at every streamwise location. Only the CLS-ARS solution duplicates the observed change in sign of $-\overline{u'v'}$ with increasing vertical distance from the wall. The isotropic eddy-viscosity models all have very similar behavior, particularly downstream.

Summary and Conclusions

A comprehensive study was performed to evaluate the performance of three explicit algebraic Reynolds-stress turbulence models for the simulation of supersonic separated flowfields. Numerical solutions were obtained for a shock/boundary-layer interaction and for the flow past a 24-deg compression ramp, both of which exhibit large regions of reversed streamwise velocity. Grid resolution studies were performed to assure numerical accuracy of the results, and solutions were compared with each other, with computations employing standard zero-equation and k–ϵ models, and with experimental data.

In terms of surface pressure and skin friction, the GS-ARS model was clearly superior to the other stress formulations. Its performance, however, was slightly worse than the SA k–ϵ representation. The GS-ARS solutions also provided the best comparison with experimental mean velocity measurements. Again though, this agreement was not better than the JL model for the shock/boundary-layer interaction or the SA model for the compression ramp.

The $\overline{u'u'}$ Reynolds-stress component was poorly predicted by all stress models in the near-wall region for the shock/boundary-layer interaction (Fig. 7) and near $\delta_0 = 1.0$ for the compression ramp (Fig. 14). Generally, the numerical levels are too low in these areas, indicating excessive turbulence energy dissipation. Predictions of $\overline{v'v'}$ are typically higher than measured values, but this component provides a much smaller contribution to the overall turbulence kinetic energy. These results indicate that some essential physics may not be replicated well by the explicit algebraic stress formulation. It is believed that at least some of this deficiency is inherent in the dissipation rate equation of the basic k–ϵ representation associated with each model.

No attempt was made to alter any of the models from their basic formulations. Some optimization of model specific constants or functions may be possible for supersonic applications, but that was considered to be beyond the scope of the present investigation. There is some evidence that turbulence production limitation or compressibility correction may be useful under certain circumstances. For the forms considered here, however, it was found that the explicit ARS models provided little improvement over other existing closures for the simulation of supersonic flows with separation. This may not necessarily be true for other practical flows of engineering interest.

Acknowledgments

The work presented here was sponsored by the U.S. Air Force Office of Scientific Research under Task 2307 AW and was monitored by L. Sakell. Computational resources were supported in part by a grant of supercomputer time from the U.S. Department of Defense Major Shared Resource Center at Vicksburg, Mississippi. The author is grateful for conversations with D. Gaitonde, who also helped identify the experimental database, and with M. R. Visbal and R. E. Gordnier. Assistance from J. H. Morrison and C. Rumsey of NASA Langley Research Center is also acknowledged.

References

[1] Abid, R., Morrison, J. H., Gatski, T. B., and Speziale, C. G., "Prediction of Complex Aerodynamic Flows with Explicit Algebraic Stress Models," AIAA Paper 96-0565, Jan. 1996.

[2] Pope, S. B., "A More General Effective Viscosity Hypothesis," *Journal of Fluid Mechanics*, Vol. 72, Pt. 2, Nov. 1975, pp. 331–340.

[3] Launder, B. E., Reece, G. J., and Rodi, W., "Progress in the Development of a Reynolds-Stress Turbulence Closure," *Journal of Fluid Mechanics*, Vol. 68, Pt. 3, 1975, pp. 537–566.

[4] Rodi, W., "The Prediction of Free Turbulent Boundary Layers by Use of a Two-Equation Model of Turbulence," Ph.D. Thesis, Mechanical Engineering Dept., Imperial College, London, Dec. 1972.

[5] Speziale, C. G., "On Nonlinear K–l and K–ϵ Models of Turbulence," *Journal of Fluid Mechanics*, Vol. 178, May 1987, pp. 459–475.

[6] Nisizima, S., and Yoshizawa, A., "Turbulent Channel and Couette Flows Using an Anisotropic k–ϵ Model," *AIAA Journal*, Vol. 25, No. 3, 1987, pp. 414–420.

[7] Rubinstein, R., and Barton, J. M., "Nonlinear Reynolds Stress Models and the Renormalization Group," *Physics of Fluids A*, Vol. 2, No. 8, 1990, pp. 1472–1476.

[8] Myong, H. K., and Kasagi, N., "Prediction of Anisotropy of the Near Wall Turbulence with an Anisotropic Low-Reynolds Number k–ϵ Turbulence Model," *Journal of Fluids Engineering*, Vol. 112, No. 4, 1990, pp. 521–524.

[9] Marvin, J. G., and Huang, G. P., "Turbulence Modeling—Progress and Future Outlook," *Proceedings of the Fifteenth International Conference on Numerical Methods in Fluid Mechanics*, Lecture Notes in Physics, edited by P. Kutler, J. Flores, and J.-J. Chatot, Springer, New York, 1997, pp. 35–56; also NASA TM 110414, Aug. 1996.

[10] Gatski, T. B., and Speziale, C. G., "On Explicit Algebraic Stress Models for Complex Turbulent Flows," *Journal of Fluid Mechanics*, Vol. 254, Sept. 1993, pp. 59–78.

[11] Speziale, C. G., and Abid, R., "Near-Wall Integration of Reynolds Stress Turbulence Closures with No Wall Damping," *AIAA Journal*, Vol. 33, No. 10, 1995, pp. 1974–1977.

[12] Abid, R., Rumsey, C., and Gatski, T., "Prediction of Nonequilibrium Turbulent Flows with Explicit Algebraic Stress Models," *AIAA Journal*, Vol. 33, No. 11, 1995, pp. 2026–2031.

[13] Abid, R., Morrison, J. H., Gatski, T. B., and Speziale, C. G., "Prediction of Aerodynamic Flows with New Explicit Algebraic Stress Model," *AIAA Journal*, Vol. 34, No. 12, 1996, pp. 2632–2635.

[14] Shih, T.-H., Zhu, J., and Lumley, J. L., "A New Reynolds Stress Algebraic Equation Model," *Computer Methods in Applied Mechanics and Engineering*, Vol. 125, Nos. 1–4, 1995, pp. 287–302.

[15] Craft, T. J., Launder, B. E., and Suga, K., "Extending the Applicability of Eddy Viscosity Models through the Use of Deformation Invariants and Non-Linear Elements," *Proceedings of the Fifth International Symposium on Refined Flow Modelling and Turbulence Measurements*, Presses Ponts et Chaussées, Paris, 1993, pp. 125–132.

[16] Craft, T. J., Launder, B. E., and Suga, K., "Development and Application of a Cubic Eddy-Viscosity Model of Turbulence," *International Journal of Heat and Fluid Flow*, Vol. 17, No. 2, 1996, pp. 108–115.

[17]Baldwin, B. S., and Lomax, H., "Thin Layer Approximation and Algebraic Model for Separated Turbulent Flows," AIAA Paper 78-257, Jan. 1978.

[18]Jones, W. P., and Launder, B. E., "The Prediction of Laminarization with a Two-Equation Model of Turbulence," *International Journal of Heat and Mass Transfer*, Vol. 15, No. 2, 1972, pp. 301–314.

[19]Jones, W. P., and Launder, B. E., "The Calculation of Low-Reynolds-Number Phenomena with a Two-Equation Model of Turbulence," *International Journal of Heat and Mass Transfer*, Vol. 16, No. 6, 1973, pp. 1119–1130.

[20]Rizzetta, D. P., "Evaluation of Algebraic Reynolds-Stress Models for Separated High-Speed Flows," AIAA Paper 97-2125, June 1997.

[21]Rizzetta, D. P., "Numerical Simulation of Slot Injection into a Turbulent Supersonic Stream," *AIAA Journal*, Vol. 30, No. 10, 1992, pp. 2434–2439.

[22]Rizzetta, D. P., "Numerical Simulation of Turbulent Cylinder Juncture Flowfields," *AIAA Journal*, Vol. 32, No. 6, 1994, pp. 1113–1119.

[23]Mundy, J. A., Rizzetta, D. P., and Melville, R. B., "Numerical Simulation of the Jet produced by an Internal Aircraft Explosion," *Journal of Aircraft*, Vol. 32, No. 2, 1995, pp. 370–376.

[24]Rizzetta, D. P., "Numerical Investigation of Supersonic Wing-Tip Vortices," *AIAA Journal*, Vol. 34, No. 6, 1996, pp. 1203–1208.

[25]Rizzetta, D. P., "Numerical Simulation of Vortex-Induced Oblique Shock-Wave Distortion," *AIAA Journal*, Vol. 35, No. 1, 1997, pp. 209–211.

[26]Beam, R., and Warming, R., "An Implicit Factored Scheme for the Compressible Navier–Stokes Equations," *AIAA Journal*, Vol. 16, No. 4, 1978, pp. 393–402.

[27]Roe, P. L., "Approximate Riemann Solvers, Parameter Vectors and Difference Schemes," *Journal of Computational Physics*, Vol. 43, No. 2, 1981, pp. 357–372.

[28]van Leer, B., "Flux-Vector Splitting for the Euler Equations," Inst. for Computer Applications in Science and Engineering, ICASE Rept. 82-30, Hampton, VA, Sept. 1982.

[29]van Leer, B., "Towards the Ultimate Conservation Difference Scheme. V. A Second-Order Sequel to Godunov's Method," *Journal of Computational Physics*, Vol. 32, No. 1, 1979, pp. 101–136.

[30]Jameson, A., Schmidt, W., and Turkel, E., "Numerical Solutions of the Euler Equations by Finite Volume Methods Using Runge–Kutta Time Stepping Schemes," AIAA Paper 81-1259, June 1981.

[31]Gordnier, R. E., and Visbal, M. R., "Numerical Simulation of Delta-Wing Roll," AIAA Paper 93-0554, Jan. 1993.

[32]Reda, D. C., and Murphy, J. D., "Shock Wave-Turbulent Boundary Layer Interactions in Rectangular Channels," AIAA Paper 72-715, June 1972.

[33]Reda, D. C., and Murphy, J. D., "Shock Wave/Turbulent Boundary-Layer Interactions in Rectangular Channels," *AIAA Journal*, Vol. 11, No. 2, 1973, pp. 139, 140.

[34]Bachalo, W. D., Modarress, D., and Johnson, D. A., "Experiments on Transonic and Supersonic Turbulent Boundary Layer Separation," AIAA Paper 77-47, Jan. 1977.

[35]Sreedhara Murthy, V., and Rose, W. C., "Wall Shear Stress Measurements in a Shock-Wave Boundary–Layer Interaction," *AIAA Journal*, Vol. 16, No. 7, 1978, pp. 667–672.

[36]Viegas, J. R., and Horstman, C. C., "Comparison of Multiequation Turbulence Models for Several Shock Boundary–Layer Interaction Flows," *AIAA Journal*, Vol. 17, No. 8, 1979, pp. 811–820.

[37]Kuntz, D. W., Amatucci, V. A., and Addy, A. L., "Turbulent Boundary-Layer Properties Downstream of the Shock-Wave/Boundary-Layer Interaction," *AIAA Journal*, Vol. 25, No. 5, 1987, pp. 668–675.

[38]Settles, G. S., and Dodson, L. J., "Hypersonic Shock/Boundary-Layer Interaction Database: New and Corrected Data," NASA CR-177638, April 1994.

C. G. Speziale
Associate Editor